Evolution of interlayer and intralayer magnetism in three atomically thin chromium trihalides

Hyun Ho Kim¹, Bowen Yang¹, Siwen Li², Shengwei Jiang³, Chenhao Jin³, Zui Tao³, George Nichols¹, Francois Sfigakis¹, Shazhou Zhong¹, Chenghe Li⁴, Shangjie Tian⁴, David G. Cory¹, Guo-Xing Miao¹, Jie Shan³, Kin Fai Mak³, Hechang Lei⁴, Kai Sun², Liuyan Zhao², and Adam W. Tsen^{1*}

¹Institute for Quantum Computing, Department of Chemistry, Department of Physics and Astronomy, and Department of Electrical and Computer Engineering, University of Waterloo, Waterloo, Ontario N2L 3G1, Canada

²Department of Physics, University of Michigan, 450 Church Street, Ann Arbor, Michigan 48109, USA

³School of Applied and Engineering Physics, Department of Physics, and Kavli Institute at Cornell for Nanoscale Science, Ithaca, NY 14853, USA

⁴Department of Physics and Beijing Key Laboratory of Opto-electronic Functional Materials & Micro-Nano Devices, Renmin University of China, Beijing 100872, China

*Correspondence to: <u>awtsen@uwaterloo.ca</u>

Abstract

We conduct a comprehensive study of three different magnetic semiconductors, CrI₃, CrBr₃, and CrCl₃, by incorporating both few- and bi-layer samples in van der Waals tunnel junctions. We find that the interlayer magnetic ordering, exchange gap, magnetic anisotropy, as well as magnon excitations evolve systematically with changing halogen atom. By fitting to a spin wave theory that accounts for nearest neighbor exchange interactions, we are able to further determine a simple spin Hamiltonian describing all three systems. These results extend the 2D magnetism platform to Ising, Heisenberg, and XY spin classes in a single material family. Using magneto-optical measurements, we additionally demonstrate that ferromagnetism can be stabilized down to monolayer in more isotropic CrBr₃, with transition temperature still close to that of the bulk.

The recent discoveries of magnetism in the monolayer limit have opened a new avenue for two-dimensional (2D) materials research¹⁻⁴. Already, several groups have reported a giant tunnel magnetoresistance effect across ultrathin CrI₃ layers⁵⁻⁸ as well as electric field control of their magnetic properties⁹⁻¹⁴. As with CrI₃, the entire family of magnetic chromium trihalides (CrX₃, X = Cl, Br, and I) possess a layered structure together with relatively strong (weak) in-plane (out-of-plane) exchange coupling¹⁵⁻²⁰, prompting a thorough investigation of the interlayer and intralayer magnetic properties of all three materials in the two-dimensional (2D) limit.

Within the layers, all three bulk compounds exhibit ferromagnetic (FM) order, although the easy axis is out-of-plane for CrI₃ and CrBr₃ and in-plane for CrCl₃. Interlayer magnetic interactions are not negligible, however, as CrI₃²¹ and CrBr₃²² are expected to exhibit FM ordering between the layers, while CrCl₃²³ shows interlayer antiferromagnetic (AFM) order in the ground state. Yet, in ultrathin CrI₃ samples, spins in adjacent layers are instead AFM coupled, giving rise to giant tunnel magnetoresistance when all layers become unipolarized by a relatively small magnetic field⁵⁻⁸. Due to the extreme sensitivity of tunnel magnetoresistance to interlayer magnetic order^{5-8, 24, 25}, we have fabricated graphite/CrX₃/graphite tunnel junctions that are fully encapsulated by hexagonal boron nitride (hBN). A schematic illustration of our devices is shown in Fig. 1a and the detailed fabrication procedure can be found in the Methods section. In brief, we exfoliated CrX₃ within a nitrogen-filled glovebox and stacked them between top and bottom graphite electrodes before encapsulation by hBN on both sides. Optical images of the devices are shown in SI Appendix, Fig. S1 and their current-voltage characteristics are shown in SI Appendix, Fig. S2.

We begin with temperature-dependent transport behavior under zero magnetic field. In Fig. 1b, we show junction resistance vs temperature upon cooling for three representative devices

incorporating the three different trihalides. Their thicknesses measured by atomic force microscopy are CrI₃: 5.6 nm, CrBr₃: 5.2 nm, and CrCl₃: 9 nm, respectively. For easy comparison, the resistances have been normalized by their minimum and maximum values and range between 0 and 1. A marked kink is observed in all devices (CrI₃: 46K, CrBr₃: 37K, and CrCl₃: 17K), close to their respective bulk magnetic transition temperatures (CrI₃: 61K²¹, CrBr₃: 37K²², and CrCl₃: 17K²³). For magnetic tunnel barriers, it has been found that the resistance either decreases or increases abruptly below the critical temperature depending on whether the magnetic ordering is FM or AFM, respectively²⁴⁻²⁶. This is caused by a spin filtering effect^{24,27}, which effectively lowers (raises) the spin-dependent tunnel barrier upon exchange splitting in the FM (AFM) state. A schematic of this effect is shown in the inset of Fig. 1b. Our devices consist of layered magnetic semiconductors in a vertical transport geometry, and therefore we expect our measurements to be most sensitive to the interlayer magnetic ordering of the few-layer samples. We thus assert that CrCl₃ and CrI₃ exhibit interlayer AFM coupling in their ground state, while CrBr₃ shows interlayer FM coupling. For CrCl₃ and CrBr₃, this is consistent with measurements of the bulk crystal, while those for CrI₃ indicate the opposite (FM coupling)²¹.

We would like to understand whether the observed interlayer magnetic ordering persists down to the ultimate limit of two atomic layers; however, the resistance kink in the temperature dependence is less apparent for thinner samples due to a smaller spin filtering effect (see SI Appendix, Fig. S3). We therefore turn to the magnetic field dependence. Here, ground state AFM and FM ordering will yield different magnetoresistance behaviors. In Figs. 2a, b, and c, we show resistance vs B_{\perp} (field perpendicular to the layers) at several different temperatures for the three bilayer (2L) CrX₃ devices. In general, the tunneling resistance is smallest when spins in adjacent layers are parallel. First, for 2L CrI₃ at low temperature (Fig. 2a), the resistance decreases abruptly

when the field exceeds ~0.75T, indicating a spin-flip transition from the AFM ground state (antiparallel out-of-plane) to a parallel spin state at higher field. This resistance change decreases with increasing temperature until it completely disappears above the magnetic transition temperature. These observations are consistent with previous findings^{5, 6}. In comparison, the resistance of 2L CrCl₃ also decreases substantially with field (Fig. 2c), reflecting that the layers are AFM coupled at zero field. The resistance evolves continuously, however, as spins point inplane in the ground state and gradually rotate with out-of-plane field. The easy axis of CrCl₃ shall be characterized and discussed in more detail later in Figs. 4 and 5. Finally, for 2L CrBr₃, the low-temperature resistance is unchanged with field (Fig. 2b), since a spin-parallel FM state has naturally formed and states with both layers spin up or down would show no difference in resistance.

In order to confirm this scenario, we have further performed magnetic circular dichroism (MCD) measurements on another 2L CrBr₃ sample (Fig. 3a). Since the MCD signal is proportional to total out-of-plane magnetization, it can resolve the difference between these two spin states with degenerate resistance. The results taken at several different temperatures are shown in SI Appendix, Fig. S4. At low temperature, a finite magnetization is observed at zero field with hysteresis between field sweep up or down, corresponding to switching of the total spin direction of the FM coupled layers. In contrast, bilayer CrI₃ shows no net magnetization at zero field as the layers are AFM coupled^{1, 5, 9-11}. The critical coercive field needed to flip the spin polarization is also much smaller for CrBr₃ (10mT at 5K). We have further performed MCD measurements on 1L, 3L, and 6L CrBr₃ and observe similar behavior (Fig 3a and SI Appendix, Fig. S4). The temperature at which the hysteresis disappears is estimated to be 27, 36, and 37K for 1L, 2L, and 3L, respectively. Interestingly, this transition temperature is not much decreased down to monolayer (Fig. 3b).

In addition to interlayer magnetic coupling, we would also like to understand the in-plane magnetic anisotropy of all three 2D compounds in greater detail. We begin with comparing the difference in magnetoresistance behaviors between perpendicular and parallel field configurations for the few-layer devices at low temperature (Figs. 4a and 4c). For CrI₃, the critical field needed to fully polarize all the spins in-plane is three times larger than that out-of-plane $(B_{\parallel}^{c} = \sim 6.5 \text{T})$ $B_{\perp}^c=\sim\!2{
m T}$). In contrast, the out-of-plane critical field is slightly larger in CrCl₃ ($B_{\parallel}^c=\sim\!2{
m T}\lesssim$ $B_{\perp}^{c} = \sim 2.4 \text{T}$). For CrBr₃, however, magnetic anisotropy cannot be directly determined by magnetoresistance since interlayer FM coupling results in nearly constant resistance independent of field orientation (see SI Appendix, Fig. S6). Instead, we compared the MCD response of fewlayer CrBr₃ for out-of-plane and in-plane field and obtain $B_{\parallel}^{c} = \sim 0.44 \text{T} \gg B_{\perp}^{c} = \sim 0.004 \text{T}$ (Fig. 4b). Additional information about the layer dependence of the critical fields can be found in SI Appendix, Section IV. These results clearly indicate that the magnetic anisotropy changes with changing halogen atom. We have further measured the full angular dependence of the tunneling current at 2T for few-layer CrI₃ and CrCl₃ (insets in Figs. 4a and 4c). Similar measurements for other magnetic field levels can be found in SI Appendix, Section V. The results show that CrI₃ exhibits the behavior of a highly anisotropic, Ising-type spin system with out-of-plane easy axis. A 2T field applied closely perpendicular to the layers fully polarizes the spins to establish a more conductive state, while the same field applied in-plane only slightly cants the spins to establish a small parallel component. While the easy axis of CrBr₃ is also out of plane, the system shows reduced anisotropy in comparison and is closer to Heisenberg. Finally, the easy axis of CrCl₃ is inplane with small anisotropy – it requires a slightly smaller field to rotate the spins within the plane than it does to fully cant them perpendicular, which suggests a weak XY spin model.

These observed differences motivate a detailed microscopic understanding of the spin

Hamiltonian for all three 2D systems, which can be extracted through observation of their excitations (magnons) at low junction biases. Towards this end, we have measured the a.c. conductance (dI/dV) vs dc voltage V of all three 2L devices using standard lock-in methods (see SI Appendix, Fig. S10). The conductance abruptly increases when the voltage reaches a magnon energy due to the opening of an additional inelastic scattering channel^{6, 28, 29}. The magnon energies can then be seen as peaks in the $|d^2I/dV^2|$ spectrum. In Fig. 5a, we show, as a color plot, the evolution of $|d^2I/dV^2|$ vs V with magnetic field along the hard axis for all three 2L trihalides, while similar data along the easy axis is shown in SI Appendix, Fig. S11a. In each case, at least two magnon modes can be seen dispersing with field. This is consistent with the underlying honeycomb lattice, which gives rise two magnon energy branches in momentum space¹⁷. The magnon density is largest at the M point. The observation of additional peaks indicates that we are resolving magnons with different momenta.

The observed magnon energies can be largely understood by considering only the intralayer magnetic interaction within a single layer. To estimate the effect of interlayer coupling, we note that the easy axis critical field for both CrI_3 and $CrCl_3$ (~2T for few layer) decreases substantially with reduced thickness (see SI Appendix, Fig. S5). In particular, it is ~0.1T for 1L CrI_3^1 . This indicates that 2T (or 0.2meV for g factor = 2) is the energy required to overcome the interlayer AFM coupling for these materials. In contrast, B_{\perp}^c maintains a small and nearly thickness independent value for $CrBr_3$, which shows interlayer FM coupling. This energy scale is an order of magnitude smaller than the observed magnon energies, and so interlayer coupling should only play a perturbative role.

The minimal model to describe ferromagnetism in a single layer of CrX₃ is the 2D anisotropic Heisenberg model, described by the Hamiltonian: $H = -J \sum_{\langle i,j \rangle} (S_i^x S_j^x + S_i^y S_j^y + S_i^y S_j^y)$

 $\alpha S_i^z S_j^z$), where $S_{i(j)}^{x(y,z)}$ is the spin operator along the x (y,z) direction at the Cr^{3+} site i (j); J is the exchange coupling constant; α is the exchange anisotropy; and $\langle i,j \rangle$ denotes the approximation of the nearest-neighbor exchange coupling. By convention, z is chosen as the direction perpendicular to the layers and J>0 for ferromagnetism. The application of a magnetic field contributes an additional Zeeman term $-g\mu_B B \sum_i S_i$ along the same spin direction.

We have performed a full spin wave analysis for monolayer CrX_3 based on the above Hamiltonian on the honeycomb lattice (see SI Appendix, Section VII). The results of which are shown in in Figs. 5b and S11b, and we now summarize. At zero field, the Γ and M point magnons have energies $\Gamma_{\pm} = \frac{9}{2}J(\alpha \pm 1)$ and $M_{\pm} = \frac{3}{2}J(3\alpha \pm 1)$. For α of order unity, $\Gamma_{-} \sim 0$ and $M_{+} \sim 2M_{-}$, restricting the magnon assignments in our data. For CrI_3 and $CrCI_3$, the most intense peaks are M_{+} and M_{-} modes, while the highest energy mode for $CrBr_3$ is assigned to be Γ_{+} , although M_{+} is also faintly visible for positive voltage. We note that for CrI_3 , this magnon assignment is consistent with a recent neutron scattering study of the bulk crystal²⁰, which shows comparable magnon energies (\sim 9 and \sim 15meV) at the M point. At other momenta, it may be important to also consider second- and third-nearest neighbor terms in the spin Hamiltonian.

When the field is applied along the easy axis (B_{\perp} for CrI₃ and CrBr₃, and B_{\parallel} for CrCl₃), all magnon energies increase linearly with field with slope $g\mu_B$. We obtain an average g factor of 2.2 between three materials. For field applied in the transverse direction (B_{\parallel} for CrI₃ and CrBr₃, and B_{\perp} for CrCl₃), the system undergoes a quantum phase transition as the spins rotate. Here, Γ_{+} and M_{\pm} modes remain nearly constant up to the anisotropy field, while Γ_{-} gets pushed to zero energy. In Fig. 5a, we indeed observe that the M_{\pm} peak positions for CrI₃ do not shift at low fields. In order

to be the difference between the critical fields applied along the hard and easy axes for the 2L devices ($B^a = 3.63$ T for CrI₃; $B^a = 0.44$ T for CrBr₃; and $B^a = 0.23$ T for CrCl₃). At high fields, all mode energies again increase by the Zeeman shift. The dashed lines in Fig. 5a and S11a guide the eye to see this change. This simple model captures the essential features of the magnon positions and dispersions for all three compounds, indicating that the data can be largely understood by considering only nearest-neighbor interactions within a single layer.

Importantly, our analysis allows us to extract both the exchange energy J and exchange anisotropy α for the 2D trihalides. In Table 1, we have summarized these values together with other key properties measured in this work. The transition temperature T_c , J, and α all decrease with smaller halogen atom. We have further measured the low-temperature, exchange gap splitting of the bandstructure E_{ex} in few-layer samples (see SI Appendix, Section VIII), which shows a similar trend. The evolving anisotropy changes the 2D spin class from Ising ($\alpha > 1$) in CrI₃, to anisotropic Heisenberg ($\alpha \ge 1$) in CrBr₃, and to weak XY ($\alpha \le 1$) in CrCl₃. Surprisingly, the transition temperature is not substantially reduced down to 1L for CrBr₃ and 2L for CrCl₃, despite the low anisotropy in these materials, indicating that strong anisotropy is not necessary to stabilize magnetism in the 2D limit.

We now end by discussing two interesting implications of these results. First, we notice that the transition temperature for bilayer CrBr₃ and CrCl₃ is already very near that of the bulk crystal, while that for few-layer CrI₃ (~46K) is still much reduced from the bulk transition temperature of 61K. It is possible that changing interlayer magnetism from FM to AFM also modifies the transition temperature of this material. In contrast, thin CrBr₃ and CrCl₃ have similar interlayer coupling with their bulk counterparts. Second, the existence and/or nature of magnetism

in monolayer CrCl₃ still remains an open question, as the 2D XY model is not expected to show long-range order at finite temperature. It may be possible that interlayer AFM coupling plays a non-negligible role in stabilizing magnetism in bilayers, although one cannot strictly rule out other more complex magnetic orders or the importance of additional in-plane exchange interactions beyond the nearest neighbor. Our work here paves the way for future studies on these topics.

Methods

Crystal synthesis. The single crystals of CrX_3 (X = Cl and I) were grown by the chemical vapor transport method. The CrX_3 polycrystals were put into the silica tube with the length of 200 mm, and inner diameter of 14mm. The tube was evacuated down to 0.01 Pa and sealed under vacuum. The tubes were placed in two-zone horizontal tube furnace and the source and growth zones were raised to 993 - 873K and 823 - 723K for 24 hours, and then held there for 150 hours. The shiny and plate-like crystals with lateral dimensions up to several millimeters can be obtained. In order to avoid degradation of CrX_3 crystals, the samples were stored in glovebox. The $CrBr_3$ single crystals were purchased from HQ graphene.

Device fabrication. Graphite (CoorsTek), h-BN (HQ graphene), CrI₃, CrBr₃ (HQ graphene), and CrCl₃ were exfoliated on polydimethylsiloxane(PDMS)-based gel (PF-40/17-X4 from Gel-Pak) within a nitrogen-filled glove box (P_{O_2} , P_{H_2O} < 0.1ppm). Pre-patterned Au (40nm)/Ti (5nm) electrodes were fabricated on 285nm-thick SiO₂/Si by using conventional photolithography and lift-off methods, and e-beam deposition. Then, vertical heterostructures of hBN/graphite/CrX₃/graphite/hBN were sequentially stacked in a home-built transfer setup inside the glove box. The overlapping area of graphite/CrX₃/graphite was set to be ~ 10 μ m². 5.6- and 7-

nm-thick CrI_3 (8 and 10 layers), 5.2- to 9-nm-thick $CrBr_3$ (8, 10, and 14 layers), and 6- to 9-nm-thick $CrCl_3$ (10, 12, and 15 layers) were used for fabrication. Thin graphite flakes were used as vertical contacts to the CrX_3 and connected to the pre-patterned electrodes, while hBN flakes were used as a passivation barrier. Devices were annealed at 393K in the glove box and were stored in vacuum desiccator until the devices were loaded into a cryostat. For bilayer CrX_3 devices, sequential pickup³⁰ was used for fabrication with $\sim 1 \ \mu m^2$ overlapping area.

Transport measurements. Transport measurement was performed in either a He4 cryostat (base temperature 1.4K) or a He3 cryostat (base temperature 0.3K). The dc current/ voltage measurements were performed with a Keithley 2450 source measure unit. A.c. tunneling measurements were performed with an additional lock-in amplifier (Stanford Research Systems SR830 with $100\mu V$ a.c. excitation and 77.77Hz frequency). A piezo rotator (atto3DR) was used to rotate the sample relative to the magnetic field.

Magneto-optical measurements. The magnetization of hBN-encapsulated CrBr₃ flakes was characterized by the magnetic circular dichroism (MCD) microscopy in a He4 cryostat (AttoDry1000) with out-of-plane magnetic field. A diode laser at 405nm with an optical power of 10μW was focused to be a sub-micron spot size on the flakes by an objective of numerical aperture 0.8. The optical excitation was modulated by a photoelastic modulator (PEM) at 50kHz for left and right circular polarization. The laser reflected from CrBr₃ was collected by the same objective and then detected by a photodiode.

Acknowledgements

AWT acknowledges support from an NSERC Discovery grant (RGPIN-2017-03815), an Ontario

Early Researcher Award (ER17-13-199), and the Korea - Canada Cooperation Program through the National Research Foundation of Korea (NRF) funded by the Ministry of Science, ICT and Future Planning (NRF-2017K1A3A1A12073407). G-XM acknowledges support from an NSERC Discovery grant (RGPIN-04178). LZ acknowledges support by NSF CAREER Grant No. DMR-1749774. The magneto-optical measurements at Cornell were supported by NSF (DMR-1807810) and ONR (award N00014-18-1-2368). This research was undertaken thanks in part to funding from the Canada First Research Excellence Fund, the National Key R&D Program of China (No. 2016YFA0300504), and the National Natural Science Foundation of China (Grant No. 11574394, 11774423, and 11822412). We thank Peter Sprenger for the assistance with cryostat operation.

Author contributions

HHK and AWT designed the experiment. HHK, BY, and SZ fabricated the devices and performed transport measurements with the assistance of GN and FS. CL, ST, and HL synthesized the bulk CrX₃ crystals. SL carried out the magnon dispersion calculation for three CrX₃ under the guidance of KS and LZ. SJ, CJ, and ZT performed MCD measurements for ultrathin CrBr₃ under the guidance of JS and KFM. DGC, G-XM, and AWT supervised. HHK and AWT wrote the paper. All authors provided comments and agreed with the final version of the manuscript.

Competing interests

The authors declare no competing interests.

References

1. Huang, B., *et al.* Layer-dependent ferromagnetism in a van der Waals crystal down to the monolayer limit. *Nature*, **546**, 270-273 (2017).

- 2. Deng, Y., *et al.* Gate-tunable Room-temperature Ferromagnetism in Two-dimensional Fe₃GeTe₂. *Nature*, **563**, 94-99 (2018).
- 3. Gong, C., *et al.* Discovery of intrinsic ferromagnetism in two-dimensional van der Waals crystals. *Nature*, **546**, 265-269 (2017).
- 4. Bonilla, M., *et al.* Strong room-temperature ferromagnetism in VSe2 monolayers on van der Waals substrates. *Nat. Nanotech.*, **13**, 289-293 (2018).
- 5. Song, T., *et al.* Giant tunneling magnetoresistance in spin-filter van der Waals heterostructures. *Science*, **360**, 1214-1218 (2018).
- 6. Klein, D. R., *et al.* Probing magnetism in 2D van der Waals crystalline insulators via electron tunneling. *Science*, **360**, 1218-1222 (2018).
- 7. Kim, H. H., *et al.* One million percent tunnel magnetoresistance in a magnetic van der Waals heterostructure. *Nano Lett.*, **18**, 4885-4890 (2018).
- 8. Wang, Z., *et al.* Very Large Tunneling Magnetoresistance in Layered Magnetic Semiconductor CrI₃. *Nat. Commun.*, **9**, 2516 (2018).
- 9. Jiang, S., Shan, J., Mak, K. F. Electric-field switching of two-dimensional van der Waals magnets. *Nat. Mater.*, **17**, 406-410 (2018).
- 10. Huang, B., *et al.* Electrical control of 2D magnetism in bilayer CrI₃. *Nat. Nanotech.*, **13**, 544-548 (2018).
- 11. Jiang, S., *et al.* Controlling magnetism in 2D CrI₃ by electrostatic doping. *Nat. Nanotech.*, **13**, 549-553 (2018).
- 12. Suarez Morell, E., León, A., Hiroki Miwa, R., Vargas, P. Control of magnetism in bilayer CrI₃ by an external electric field. *2D Mater.* **6**, 025020 (2019).
- 13. Jiang, S., *et al.* Spin tunnel field-effect transistors based on two-dimensional van der Waals heterostructures. *Nat. Electron.* **2**, 159-163 (2019).
- 14. Song, T., *et al.* Voltage control of a van der Waals spin-filter magnetic tunnel junction. *Nano Lett.* **19**, 915-920 (2019).
- 15. Liu, J., Sun, Q., Kawazoe, Y., Jena, P. Exfoliating biocompatible ferromagnetic Crtrihalide monolayers. *Phys. Chem. Chem. Phys.*, **18**, 8777-8784 (2016).
- 16. Lado, J. L., Fernández-Rossier, J. On the origin of magnetic anisotropy in two dimensional CrI₃. *2D Mater.*, **4**, 035002 (2017).
- 17. Jin, W., *et al.* Raman fingerprint of two terahertz spin wave branches in a two-dimensional honeycomb Ising ferromagnet. *Nat. Commun.*, **9**, 5122 (2018).

- 18. Zhang, W.-B., Qu, Q., Zhu, P., Lam, C.-H. Robust intrinsic ferromagnetism and half semiconductivity in stable two-dimensional single-layer chromium trihalides. *J. Mater. Chem. C*, **3**, 12457-12468 (2015).
- 19. Feldkemper, S., Weber, W. Generalized calculation of magnetic coupling constants for Mott-Hubbard insulators: Application to ferromagnetic Cr compounds. *Phys. Rev. B*, **57**, 7755-7766 (1998).
- 20. Chen, L., *et al.* Topological Spin Excitations in Honeycomb Ferromagnet CrI₃. *Phys. Rev. X*, **8**, 041028 (2018).
- 21. McGuire, M. A., Dixit, H., Cooper, V. R., Sales, B. C. Coupling of Crystal Structure and Magnetism in the Layered, Ferromagnetic Insulator CrI₃. *Chem. Mater.*, **27**, 612-620 (2015).
- 22. Tsubokawa, I. On the Magnetic Properties of a CrBr₃ Single Crystal. *J. Phys. Soc. Jpn.*, **15**, 1664-1668 (1960).
- 23. McGuire, M. A., *et al.* Magnetic behavior and spin-lattice coupling in cleavable van der Waals layered CrCl₃ crystals. *Phys. Rev. Mater.*, **1**, 014001 (2017).
- 24. Hao, X., Moodera, J. S., Meservey, R. Spin-filter effect of ferromagnetic europium sulfide tunnel barriers. *Phys. Rev. B*, **42**, 8235-8243 (1990).
- 25. Santos, T. S., *et al.* Determining Exchange Splitting in a Magnetic Semiconductor by Spin-Filter Tunneling. *Phys. Rev. Lett.*, **101**, 147201 (2008).
- 26. Esaki, L., Stiles, P. J., Molnar, S. v. Magnetointernal Field Emission in Junctions of Magnetic Insulators. *Phys. Rev. Lett.*, **19**, 852-854 (1967).
- 27. Miao, G.-X., Müller, M., Moodera, J. S. Magnetoresistance in Double Spin Filter Tunnel Junctions with Nonmagnetic Electrodes and its Unconventional Bias Dependence. *Phys. Rev. Lett.*, **102**, 076601 (2009).
- 28. Ghazaryan, D., *et al.* Magnon-assisted tunnelling in van der Waals heterostructures based on CrBr₃. *Nat. Electron.*, **1**, 344-349 (2018).
- 29. Tsui, D. C., Dietz, R. E., Walker, L. R. Multiple Magnon Excitation in NiO by Electron Tunneling. *Phys. Rev. Lett.*, **27**, 1729-1732 (1971).
- 30. Wang, L., *et al.* One-Dimensional Electrical Contact to a Two-Dimensional Material. *Science*, **342**, 614-617 (2013).

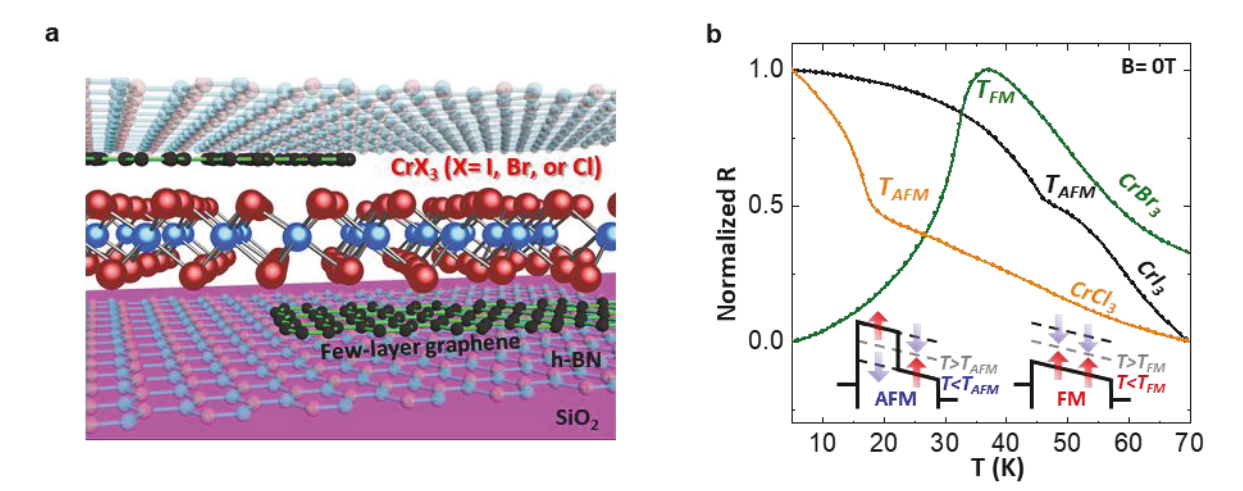


Figure 1. Magnetic van der Waals tunnel junction incorporating ultrathin chromium trihalides. (a) Schematic illustration of the device. (b) Normalized temperature-dependent dc resistance of CrX_3 (X=I, Br, and CI) at constant current of 0.1nA. Insets show schematics of the spin-dependent tunnel barrier for AFM and FM interlayer coupling. Red and blue arrows indicate spin orientation and are used throughout.

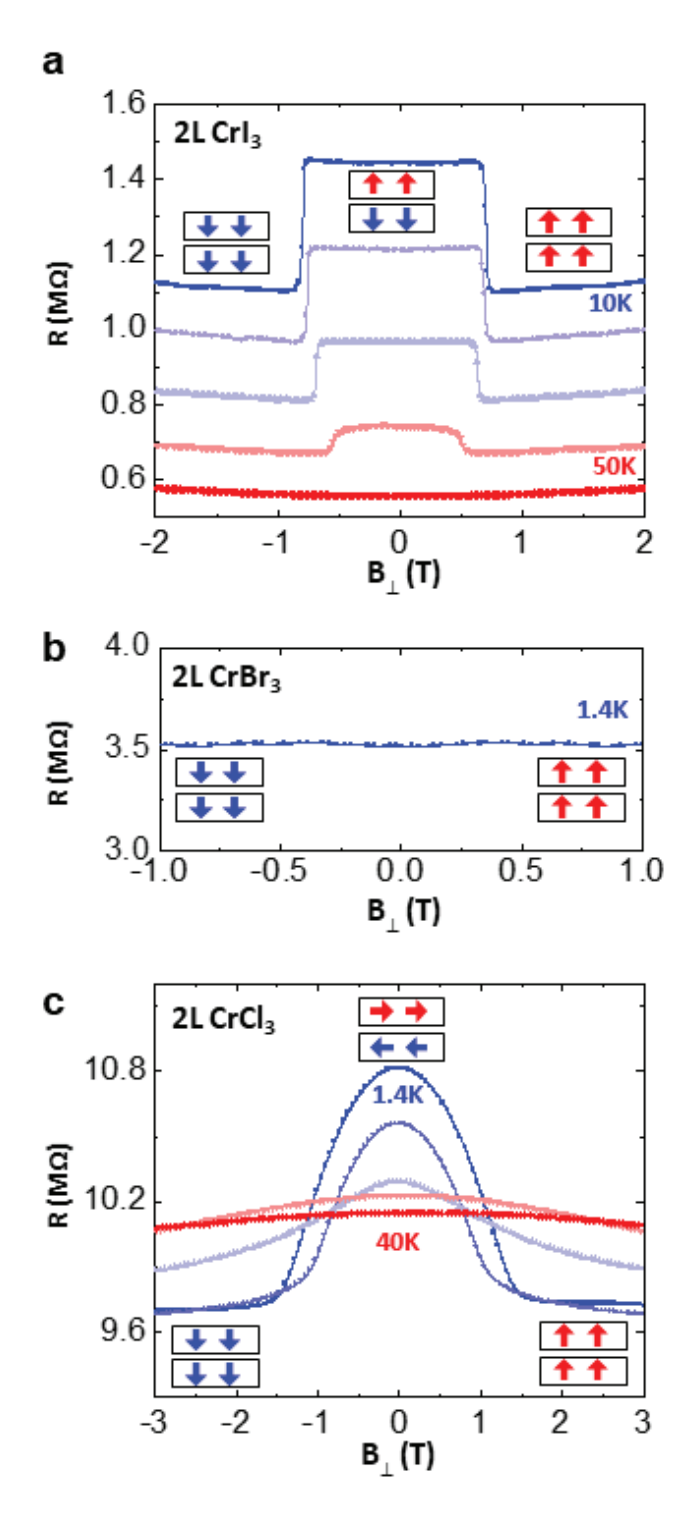


Figure 2. Tunneling probe of interlayer magnetic coupling in bilayer CrX_3 . Resistance vs B_{\perp} of (a) $2L\ CrI_3$ taken at 10, 20, 30, 40, and 50K, in sequence from blue to red (b) $2L\ CrBr_3$ at 1.4K, and (c) $2L\ CrCl_3$ at 1.4, 10, 20, 30 and 40K. in the sequence from blue to red.

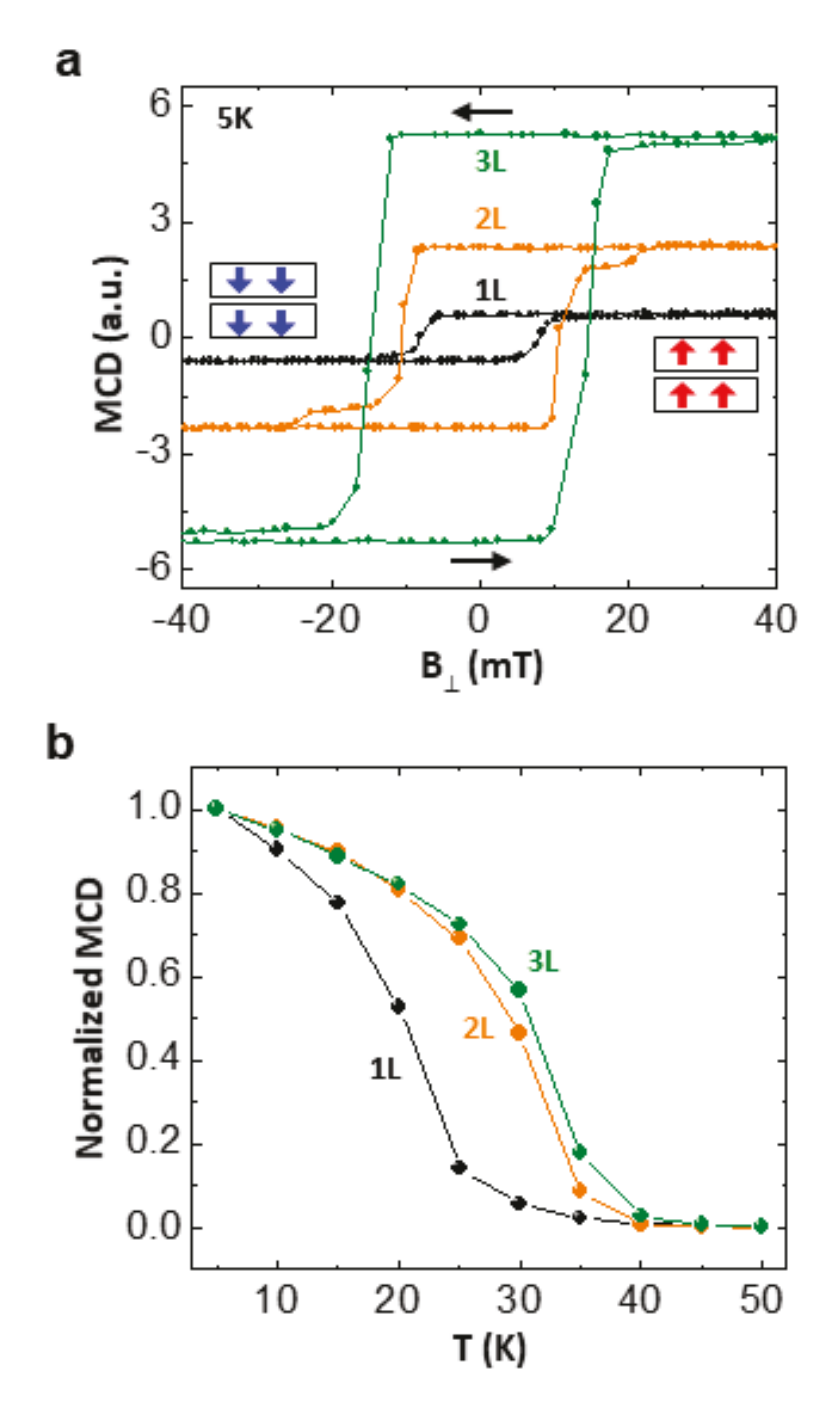


Figure 3. Magnetic circular dichroism (MCD) measurements on CrBr₃. (a) Low-temperature MCD vs B_{\perp} and (b) temperature-dependent normalized MCD at zero field $(\frac{MCD_{\uparrow(\downarrow)}(T)}{MCD_{\uparrow(\downarrow),5K}})$ for 1L, 2L, and 3L CrBr₃.

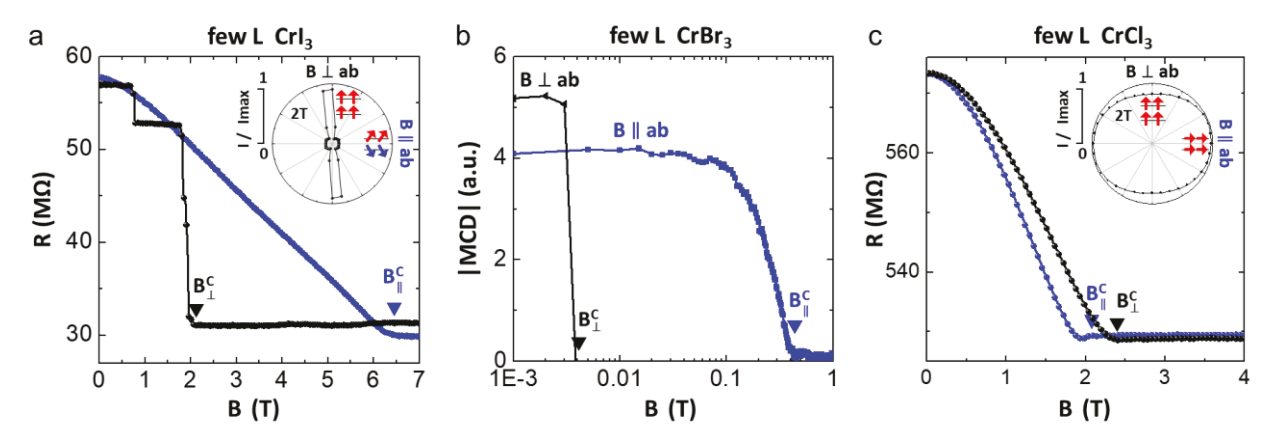


Figure 4. Magnetic anisotropy in few-layer CrX₃. Comparison of magnetoresistance (1nA current biasing at 1.4K) of (a) 8L CrI₃ and (c) 15L CrCl₃ for perpendicular and parallel magnetic field directions. (b) |MCD| vs B of 3L CrBr₃ at 1.6K for the two field directions. Insets in (a) and (c) show angle-dependent, normalized tunneling current (voltage biasing, 0.5V for CrI₃, and 5.7V for CrCl₃) at 2T.

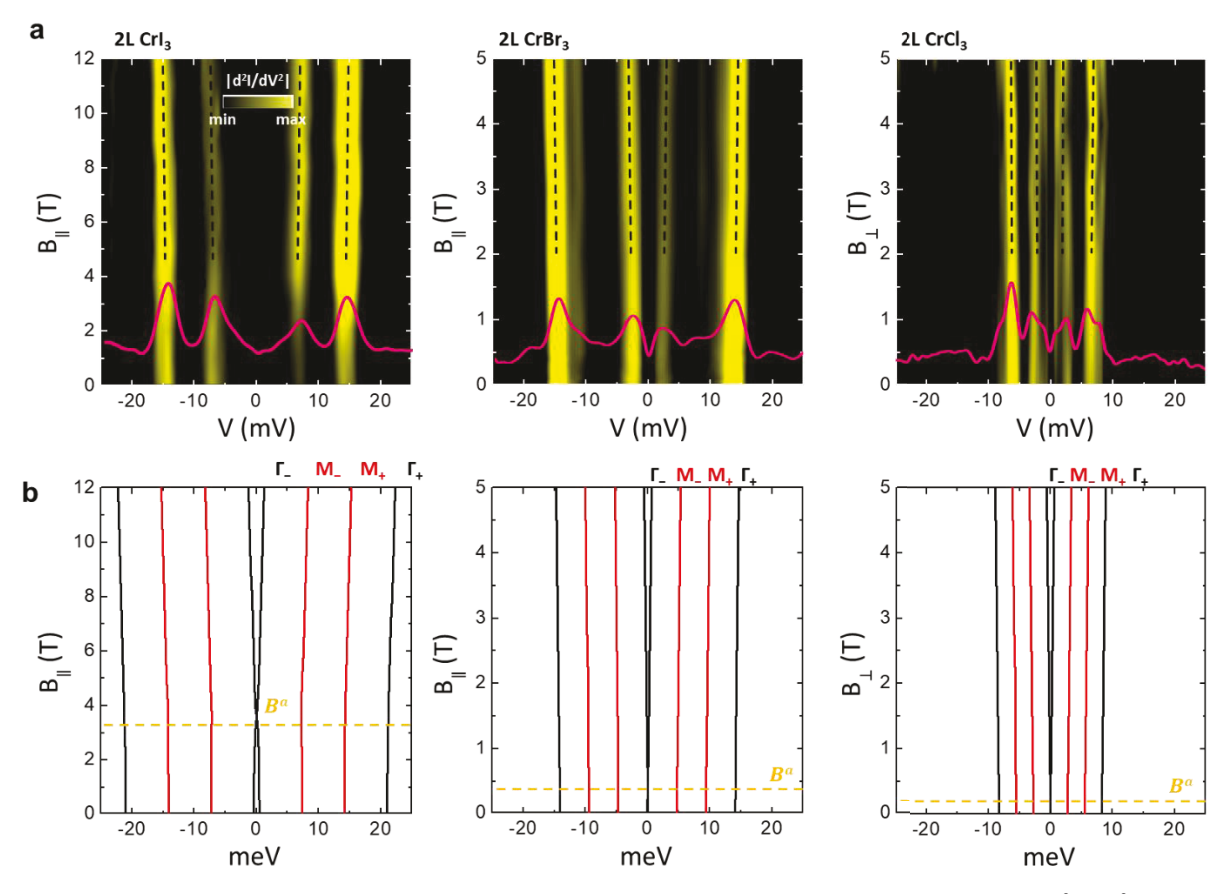


Figure 5. Inelastic tunneling spectroscopy of magnons in bilayer CrX_3 . (a) Field-dependent $|d^2I/dV^2|$ vs voltage for $2L CrX_3$ at 0.3K and (b) calculated magnon energies for $1L CrX_3$ with magnetic field applied along the hard axis. Magnon peaks in (a) are partially guided by dashed lines.

Table 1. Summary of magnetic properties of 2D CrX₃

	Crl ₃	CrBr ₃	CrCl ₃
Interlayer magnet coupling	ic AFM	FM	AFM
т _с (к)	Few L: 46 (tunneling) 2L: 45 (tunneling) 1L: 45 (MOKE) ^{1,11}	Few L: 37 (tunneling) 3L: 37 (MCD) 2L: 36 (MCD) 1L: 27 (MCD)	Few L: 17 (tunneling) 2L: 16 (tunneling)
E _{ex} (meV)	136	122	68
J (meV)	2.29	1.56	0.92
α	1.04	1.01	0.99
Spin model	Ising	Anisotropic Heisenberg	Weak XY

Supporting Information for

Evolution of interlayer and intralayer magnetism in three atomically thin chromium trihalides

Hyun Ho Kim¹, Bowen Yang¹, Siwen Li², Shengwei Jiang³, Chenhao Jin³, Zui Tao³, George Nichols¹, Francois Sfigakis¹, Shazhou Zhong¹, Chenghe Li⁴, Shangjie Tian⁴, David G. Cory¹, Guo-Xing Miao¹, Jie Shan³, Kin Fai Mak³, Hechang Lei⁴, Kai Sun², Liuyan Zhao², and Adam W. Tsen^{1*}

¹Institute for Quantum Computing, Department of Chemistry, Department of Physics and Astronomy, and Department of Electrical and Computer Engineering, University of Waterloo, Waterloo, Ontario N2L 3G1, Canada

²Department of Physics, University of Michigan, 450 Church Street, Ann Arbor, Michigan 48109,USA

³School of Applied and Engineering Physics, Department of Physics, and Kavli Institute for Nanoscale Science, Cornell University, Ithaca, New York 14853, USA

⁴Department of Physics and Beijing Key Laboratory of Opto-electronic Functional Materials & Micro-Nano Devices, Renmin University of China, Beijing 100872, China

*Correspondence to: <u>awtsen@uwaterloo.ca</u>

I. Fabrication of CrX3 devices

Optical images of CrX₃ devices were taken just before top hBN passivation, as shown in Fig. S1. Cracks and wrinkles were avoided during the fabrication. For few-layer devices, we used the sequential transfer method with PDMS as our previous work¹. Conventional pickup process using poly(bisphenol A carbonate) thin film² was used for the fabrication of bilayer devices due to a cracking issue.

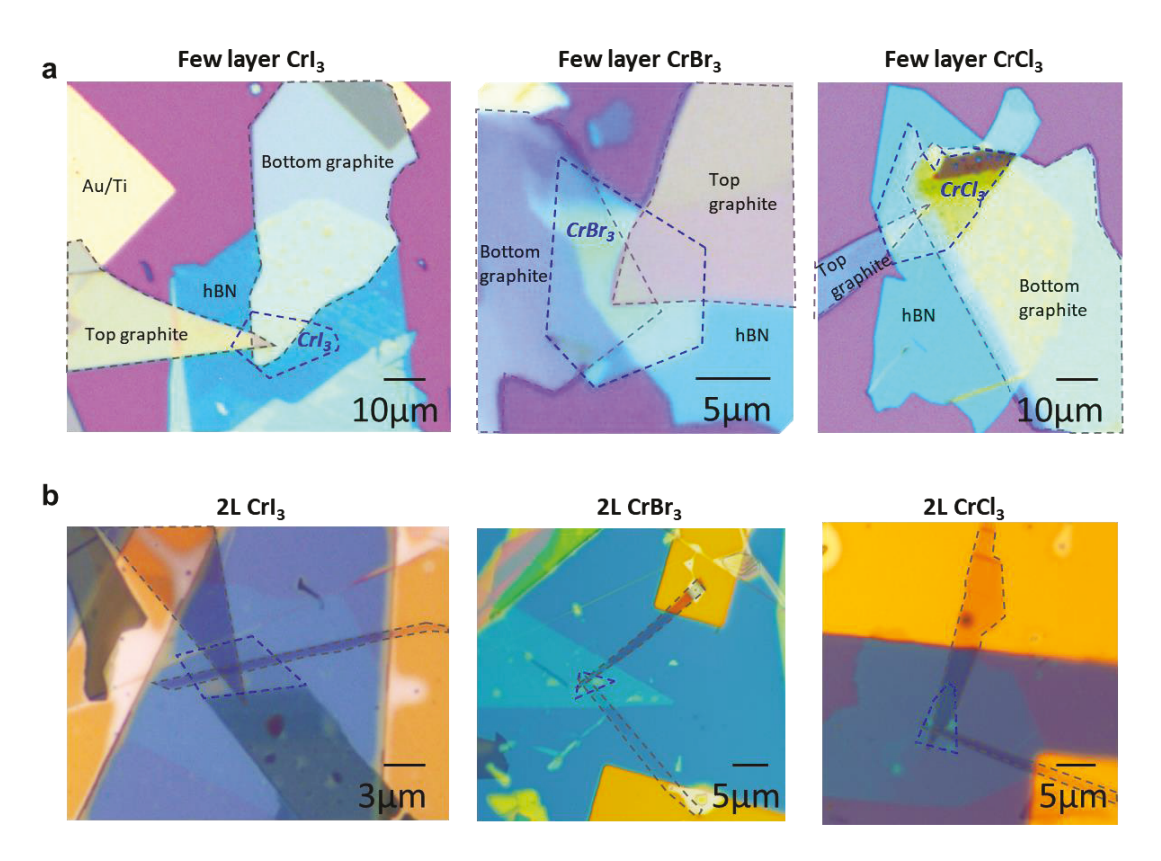


Figure S1. Optical images of vertical van der Waals magnetic tunnel junction devices. (a) 8-layer CrI₃, 14-layer CrBr₃, and 15-layer CrCl₃ (before covering top h-BN). (b) complete 2L CrX₃ devices.

II. Additional information for temperature dependence

In Fig. S2a, we show nonlinear current-voltage behavior characteristics of few-layer CrX_3 magnetic tunnel junctions. Below the magnetic transition temperature (T_{AFM} and T_{FM}), current at fixed voltage decreases as the temperature decreases in CrI_3 and $CrCl_3$ devices, whereas $CrBr_3$ shows a reverse tendency. Bilayer devices exhibit near ohmic behavior in CrI_3 and $CrBr_3$, indicating that direct tunneling is dominant rather than Fowler-Nordheim (FN) tunneling. Since the bandgap is expected to be large in $CrCl_3$, we could still measure FN tunneling starting from $\sim 1V$. Due to this effect, clear spin-filtering can still be observed in 2L $CrCl_3$ devices, but not in 2L CrI_3 or 2L $CrBr_3$, as shown in Fig. S3.

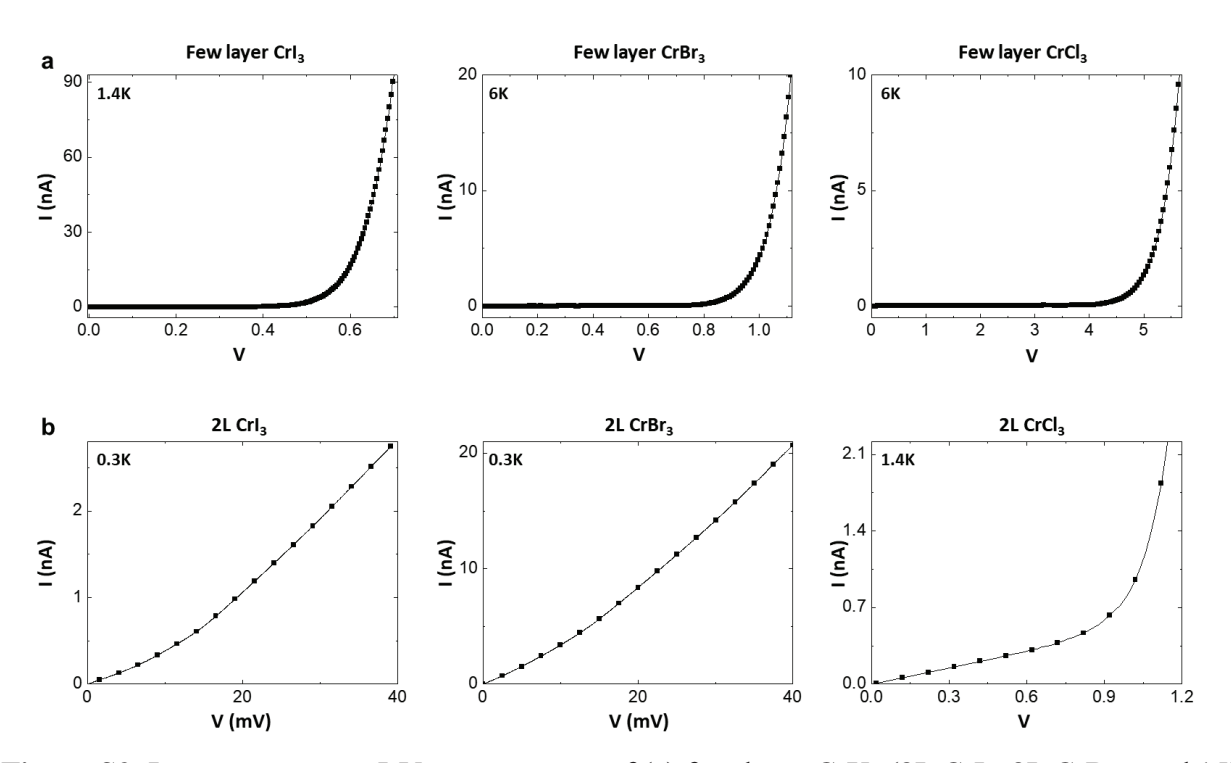


Figure S2. Low-temperature I-V measurement of (a) few-layer CrX₃ (8L CrI₃, 8L CrBr₃, and 15L CrCl₃. And (b) 2L CrX₃.

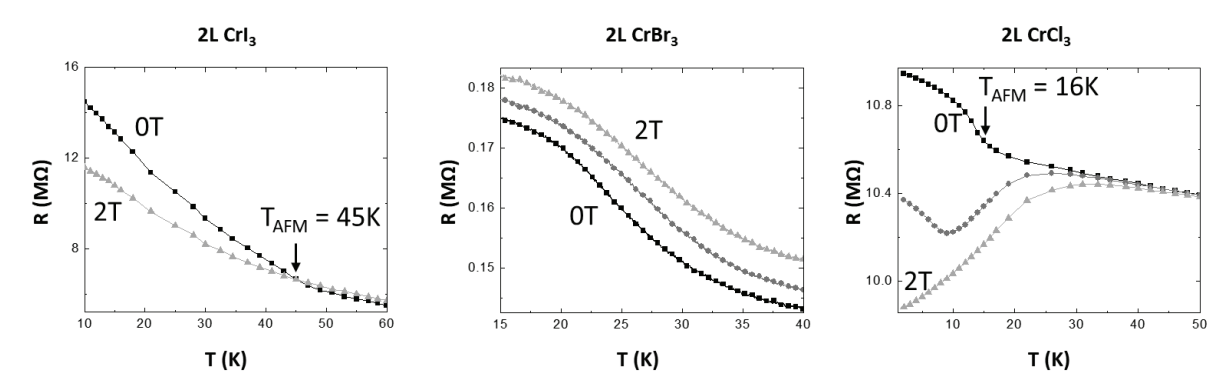


Figure S3. Resistance vs temperature as a function of perpendicular field (0, 1, and 2T) for three bilayer CrX_3 devices.

III. Magnetic circular dichroism measurements on CrBr₃

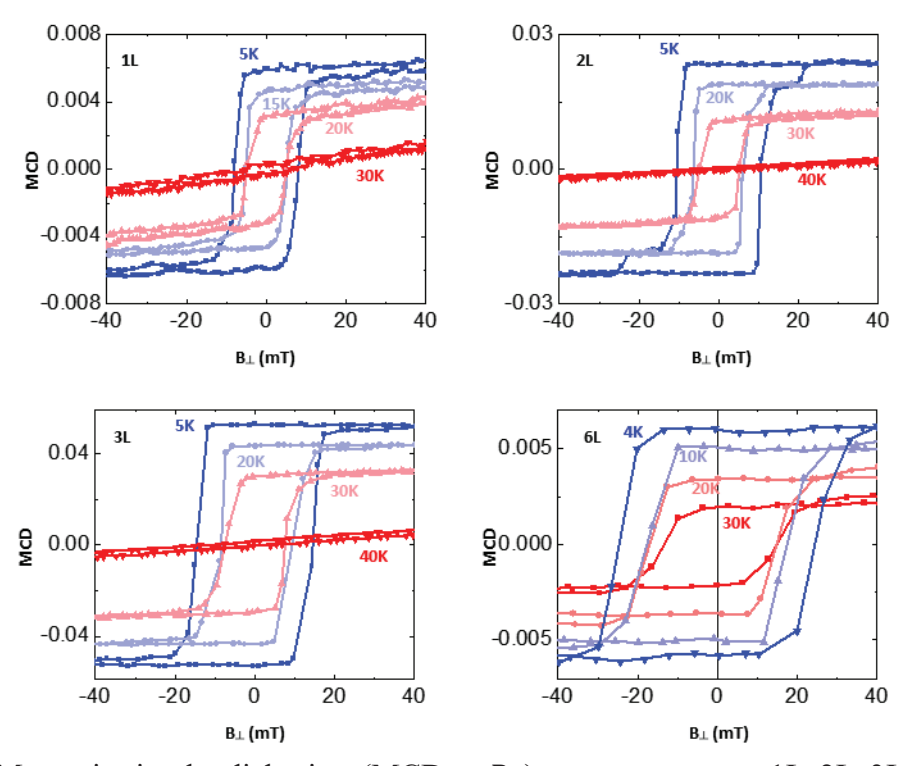


Figure S4. Magnetic circular dichroism (MCD vs B_{\perp}) measurements on 1L, 2L, 3L, and 6L CrBr₃.

IV. Layer-dependent critical field of CrX3

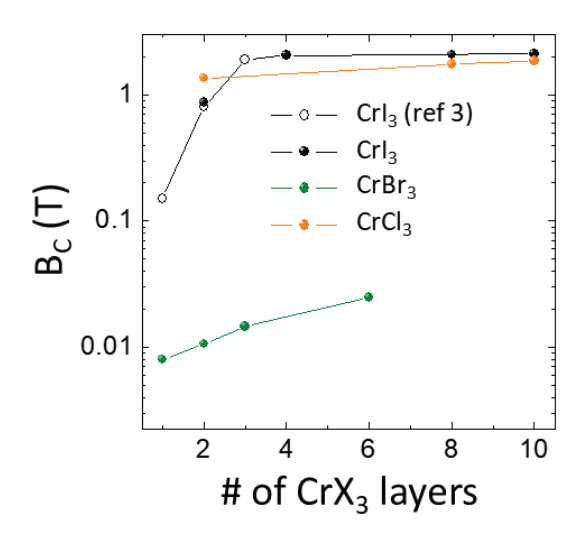


Figure S5. Critical field (B_C) of CrX₃ as a function of the number of layers along with easy axis. CrI₃ and CrBr₃ were measured with perpendicular field and CrCl₃ was measured with parallel field. It is noted that critical fields for CrI₃ and CrCl₃ above 2L show relatively higher values due to the interlayer AFM coupling.

V. Additional information for magnetic anisotropy

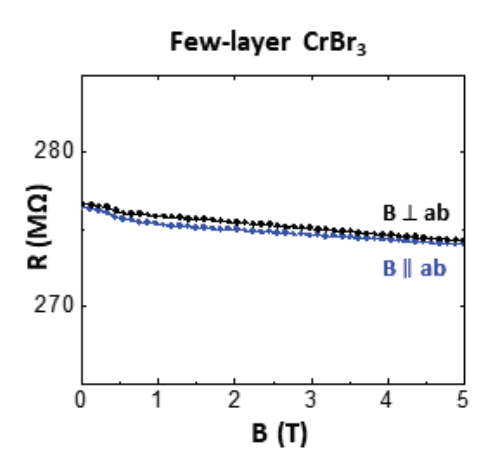


Figure S6. Comparison of magnetoresistance (1nA current biasing at 1.4K) of 10L CrBr₃.

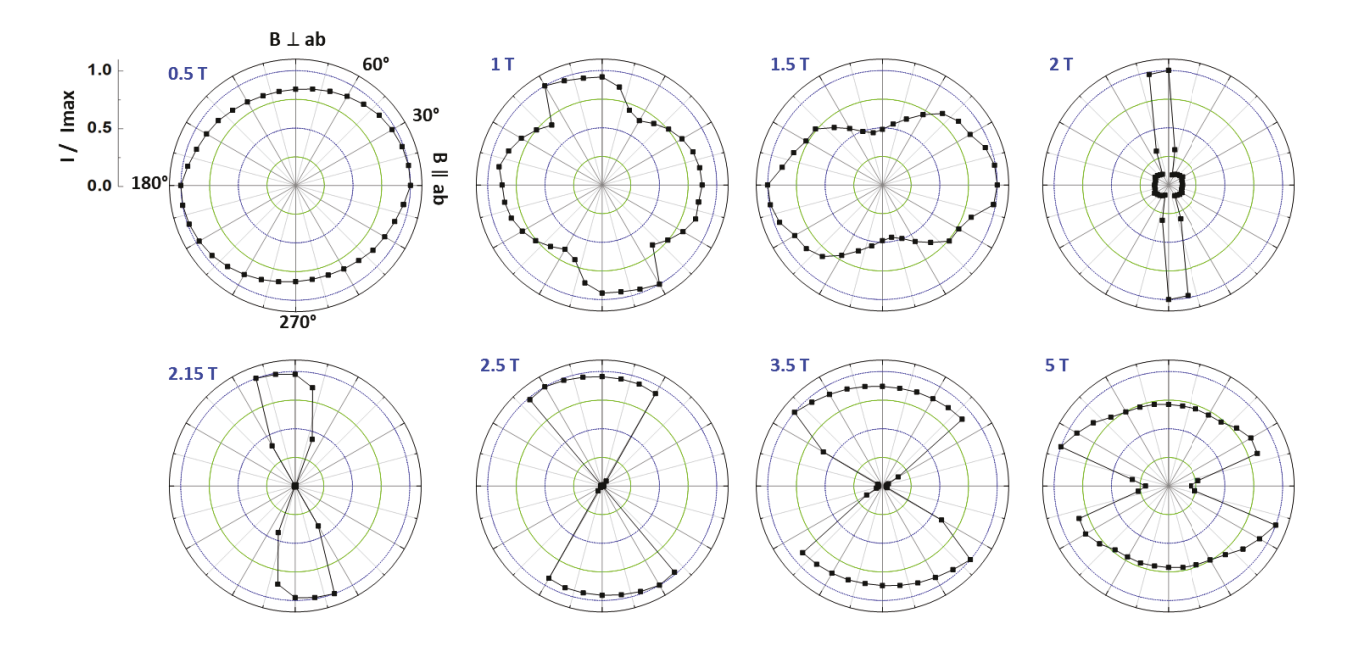


Figure S7. Theta-and field-dependent normalized tunnel current of 8-layer CrI₃ from 0.5 to 5T.

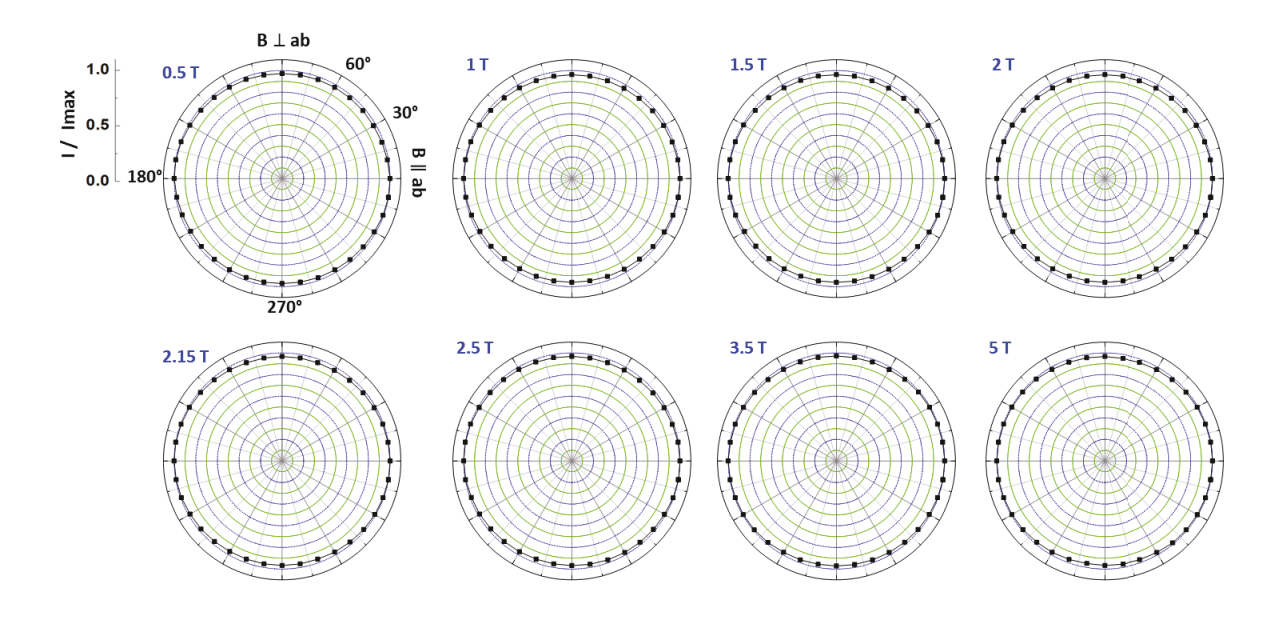


Figure S8. Theta-and field-dependent normalized tunnel current of 10-layer CrBr₃ from 0.5 to 5T.

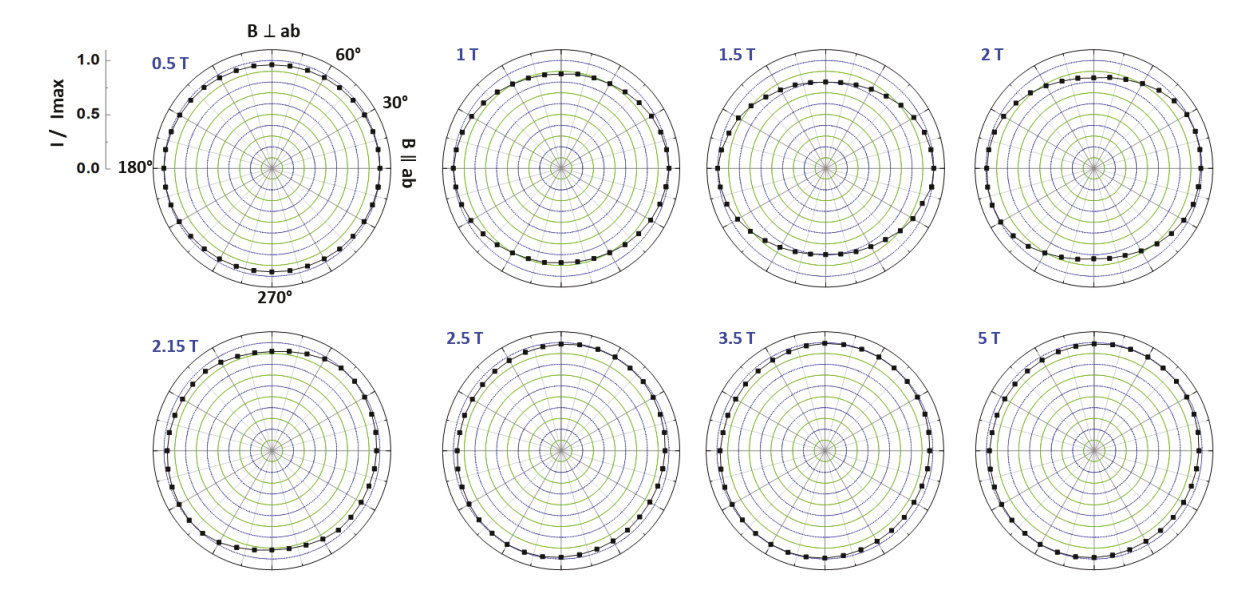


Figure S9. Theta-and field-dependent normalized tunnel current of 15-layer CrCl₃ from 0.5 to 5T.

VI. Additional information for inelastic tunneling spectroscopy

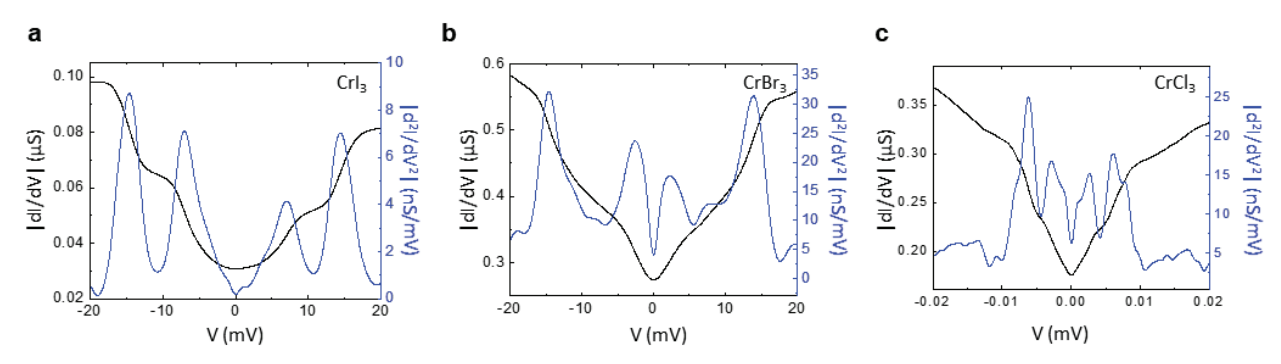


Figure S10. The ac conductance (G, dI/dV) vs dc voltage of (a) 2L CrI₃, (b) 2L CrBr₃, and (c) 2L CrCl₃. The derivative $|d^2I/dV^2|$ is shown in blue solid line. Conductance at each dc voltage is measured with 100 μ V ac excitation voltage.

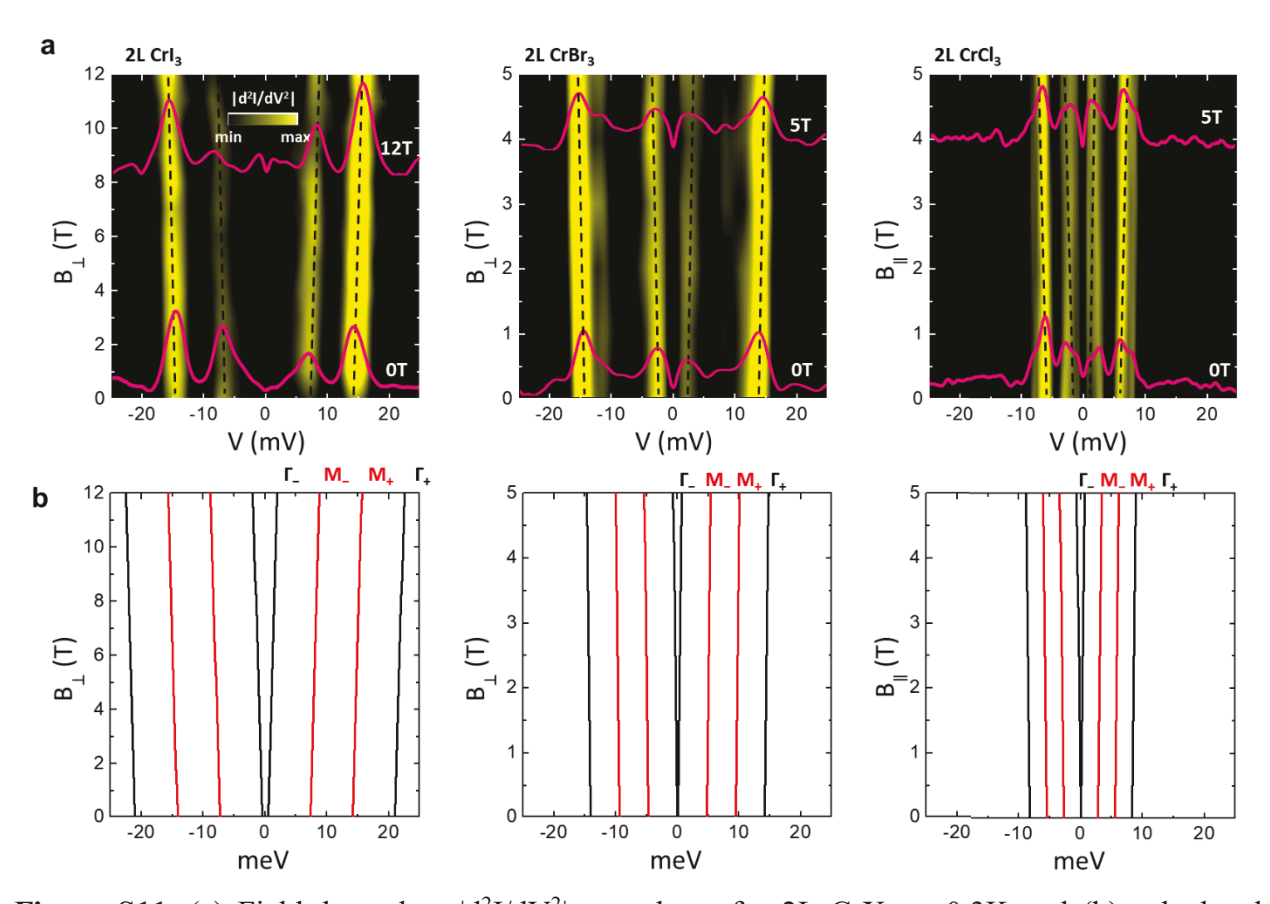


Figure S11. (a) Field-dependent $|d^2I/dV^2|$ vs voltage for 2L CrX₃ at 0.3K and (b) calculated magnon energies for 1L CrX₃ with field applied along the easy axis. Magnon peaks in (a) are guided by dashed lines.

VII. Spin wave calculations under an external magnetic field

In the following, we perform calculations of spin wave dispersions under an external magnetic field for monolayer honeycomb magnets CrX₃. Our spin Hamiltonian only considers monolayer spin structure instead of the actual bilayer structure, because interlayer interactions are small compared to intralayer exchange interactions. Although bilayer splitting modifies the monolayer spin wave dispersions, it seems unnecessary in evaluating intralayer exchange interactions. We choose the anisotropic Heisenberg spin model below,

$$H = -J \sum_{\langle i,j \rangle} \left(S_i^x S_j^x + S_i^y S_j^y + \alpha S_i^z S_j^z \right) - g \mu_B \left(B_z \sum_i S_i^z + B_x \sum_i S_i^x \right)$$

where J is the nearest neighbor exchange energy, i and j denote the two inequivalent Cr^{3+} site, and α scales the z-direction exchange strength. In particular, α is greater than, equivalent to, or smaller than 1 for Ising, isotropic Heisenberg, or XY magnets, respectively. g is the g-factor for Cr^{3+} magnetic moments, μ_B is the Bohr magneton, and \vec{B} is external magnetic field. Depending on the experimental geometry, either B_z or B_x is nonzero, representing the magnetic field perpendicular to or parallel to the plane of CrX_3 layers.

Without an external magnetic field, the spins in CrX_3 align either along the z-axis or in the xy-plane depending on the magnitude of α . When an external field is applied perpendicular to the easy axis or easy plane, it tilts the spins off its original direction, to a new direction that minimizes the energy for the Hamiltonian above. To keep it general for all three types of magnets, we characterize the spin orientation by its tilt angle from z axis, θ . For example, $\theta = 0$ corresponds to the spins aligning along the z-axis and $\theta = \pi/2$ for spins in the xy-plane. To determine θ for a given external magnetic field, a rotation transform is applied, where \vec{S} is the spin orientation in the new ground state under the external field:

$$\begin{cases} S^{x} = \tilde{S}^{x} cos\theta + \tilde{S}^{z} sin\theta \\ S^{z} = -\tilde{S}^{x} sin\theta + \tilde{S}^{z} cos\theta \end{cases}$$

After applying Holstein-Primakoff transform for both site *i* and site *j*,

$$\begin{cases} \tilde{S}^z = S - a^{\dagger} a \\ \tilde{S}^+ = \sqrt{2S} (1 - \frac{a^{\dagger} a}{2S}) a \\ \tilde{S}^- = \sqrt{2S} a^{\dagger} \end{cases}$$

we arrive at the following Hamiltonian where spin wave interactions are ignored:

$$H = H_{const} + H_1 + H_2$$

$$H_{const} = -SN(JzS(\alpha \cos^2 \theta + \sin^2 \theta) + 2g\mu_B(\sin\theta B_x + \cos\theta B_z))$$

$$H_1 = (\frac{1}{2}JSz(\alpha - 1)\sin 2\theta + g\mu_B(B_z\sin\theta - B_x\cos\theta))\sqrt{S/2}\sum_i (a_i^{\dagger} + a_i)$$

$$H_2 = -\frac{1}{2}JS(\alpha \sin^2 \theta + \cos^2 \theta - 1)\sum_{\langle i,j \rangle} (a_i^{\dagger} b_j^{\dagger} + a_i b_j)$$

$$-\frac{1}{2}JS(\alpha \sin^2 \theta + \cos^2 \theta + 1)\sum_{\langle i,j \rangle} (a_i^{\dagger} b_j + a_i b_j^{\dagger})$$

$$+ JS(\alpha \cos^2 \theta + \sin^2 \theta)\sum_{\langle i,j \rangle} (a_i^{\dagger} a_i + b_j^{\dagger} b_j)$$

$$+ g\mu_B(\sin\theta B_x + \cos\theta B_z)(\sum_i a_i^{\dagger} a_i + \sum_i b_j^{\dagger} b_j)$$

where N is the number of sublattices, and z is the number of nearest neighbor spins. Minimizing H_{const} yields the new spin orientation θ and eliminates H_1 . If \vec{B} is parallel to the original spin orientation, the spins remain the same. If \vec{B} is perpendicular, θ is a function of $|\vec{B}|$. At low fields,

$$\theta = arcsin \frac{g\mu_B B_x}{JSz(\alpha - 1)} \ (B_z = 0, \alpha > 1)$$

and

$$\theta = \arccos \frac{g\mu_B B_z}{JSz(1-\alpha)} \ (B_x = 0, \alpha < 1)$$

A critical field strength B_c exists above which the spins are completely aligned along the external field direction.

To obtain the spin wave dispersions under external magnetic fields, Fourier and Bogoliubov transforms of spin wave operators are applied to H_2 . Fourier transform yields

$$H_{2} = Q_{1} \sum_{k} (a_{k}^{\dagger} b_{-k}^{\dagger} \gamma_{-k} + a_{k} b_{-k} \gamma_{k}) + Q_{2} \sum_{k} (a_{k}^{\dagger} b_{k} \gamma_{-k} + a_{k} b_{k}^{\dagger} \gamma_{k})$$
$$+ Q_{3} \sum_{k} (a_{k}^{\dagger} a_{k} + b_{k}^{\dagger} b_{k})$$

where

$$\gamma_k = \frac{1}{z} \sum_{\delta} e^{ik\delta}$$

$$Q_1 = -\frac{1}{2} JSz(\alpha \sin^2 \theta + \cos^2 \theta - 1)$$

$$Q_2 = -\frac{1}{2} JSz(\alpha \sin^2 \theta + \cos^2 \theta + 1)$$

$$Q_3 = JSz(\alpha \cos^2 \theta + \sin^2 \theta) + g\mu_B(\sin\theta B_x + \cos\theta B_z)$$

 a_k and b_k correspond to the Fourier transformed spin wave operators of real space operators a_i and b_i , respectively. Bogoliubov transform for bosonic excitations is then done by

$$\begin{pmatrix} \phi_{-k} \\ \psi_{-k} \\ \phi_k^{\dagger} \\ \psi_k^{\dagger} \end{pmatrix} = M \begin{pmatrix} a_{-k} \\ b_{-k} \\ a_k^{\dagger} \\ b_k^{\dagger} \end{pmatrix}$$

$$M = \begin{pmatrix} \frac{Q_3 - Q_2 P_1 - P_2}{Q_1 \gamma_k} & -\frac{Q_3 - Q_2 P_1 - P_2}{Q_1 P_1} & -\sqrt{\frac{\gamma_{-k}}{\gamma_k}} & 1 \\ \frac{Q_3 + Q_2 P_1 - P_3}{Q_1 \gamma_k} & \frac{Q_3 + Q_2 P_1 - P_3}{Q_1 P_1} & \sqrt{\frac{\gamma_{-k}}{\gamma_k}} & 1 \\ \frac{Q_3 - Q_2 P_1 + P_2}{Q_1 \gamma_k} & -\frac{Q_3 - Q_2 P_1 + P_2}{Q_1 P_1} & -\sqrt{\frac{\gamma_{-k}}{\gamma_k}} & 1 \\ \frac{Q_3 + Q_2 P_1 - P_3}{Q_1 \gamma_k} & \frac{Q_3 + Q_2 P_1 - P_3}{Q_1 P_1} & \sqrt{\frac{\gamma_{-k}}{\gamma_k}} & 1 \end{pmatrix}$$

where

$$P_1 = \sqrt{\gamma_k \gamma_{-k}}$$

$$P_2 = \sqrt{Q_3^2 - 2Q_3 Q_2 P_1 + (Q_2^2 - Q_1^2) P_1^2}$$

$$P_3 = \sqrt{Q_3^2 + 2Q_3 Q_2 P_1 + (Q_2^2 - Q_1^2) P_1^2}$$

M is the Bogoliubov transform matrix under which the new operators ϕ_k and ψ_k satisfy bosonic commutation relations (up to a normalization factor). Spin wave dispersions as a function of external field strength are obtained as $E_1 = P_2$, and $E_2 = P_3$. If \vec{B} is parallel to the original spin orientation, spin wave energies increase by $g\mu_B |\vec{B}|$. If \vec{B} is perpendicular, spin wave energies show an anomaly at B_c , as shown in the main text Figure 5.

Input parameters and fit with experimental data

For Cr^{3+} , the spin moment has S=3/2. In the honeycomb lattice, the number of nearest neighbors is z=3. At large fields, the spin wave energies increase by $g\mu_B B$. g-factor is then extracted from the slope of the spin wave energies as a function of external field. g is taken to be

2.1788, which is the average of the slopes of all three compounds. The spin wave density of states is high at Γ - and M-point, so that the experimentally observed peaks are related with two Γ -point excitations and two M-point excitations. We use the transition fields B_c from the field dependent tunneling spectroscopy data to find a relation between J and α , and identify their values fitting the calculated functional forms to the experimental results.

Table S1 lists B_c from experiment and J and α from fitting results.

Table S1. Spin wave parameters in CrX₃ compounds

Compound	B_{c} (T)	J (meV)	α
CrI ₃	3.63	2.286	1.0445
CrBr ₃	0.44	1.562	1.0079
CrCl ₃	0.23	0.9208	0.9930

VIII. Estimation of spin-splitting energy

In the top panel of Fig. S12a, we show how to deduce the exchange energy gap from the current-voltage characteristics. As described in a previous report¹, the spin-slitting energy gap (E_{ex}) can be approximated by taking barrier height difference between fully polarized P state and paramagnetic state (PM), $E_{ex} = 2(\Phi_{PM} - \Phi_{P})$. Barrier height is calculated in Fowler-Nordheim³ regime using the current-voltage relation:

$$J = \left(\frac{e^3 E^2}{4\hbar\Phi}\right) \exp\left(-\frac{4\sqrt{2m\Phi^3}}{3\hbar eE}\right)$$

where e is electronic charge, E is the electric field across the CrX₃, m is the effective electron mass, which we estimate to be the free-electron mass, \hbar is the Planck's constant, and Φ is the barrier height between the thin graphite electrode and CrX₃. In the bottom panel of Fig. S12a, we plot representative $\ln(J/E^2)$ vs E^{-1} for a 10-layer CrI₃ in both the PM state (at 49K with B=0) and fully polarized state (at 1.4K with B₁ = 5.5T). We found that the negative slope proportional to $\Phi^{3/2}$ becomes flatter from PM to fully parallel state. As shown in Fig. S12b, the splitting energies of few-layer CrX₃ are estimated to be CrI₃ ~136meV, CrBr₃ ~122meV, and CrCl₃ ~68meV. While these values are slightly smaller than those from bandstructure calculations⁴, the trend with changing halogen size is consistent. At the same time, we also observed different initial barrier heights in PM state (~227meV in CrI₃, ~538meV in CrBr₃, and ~943meV in CrCl₃), which is consistent with calculations showing increasing bandgap with decreasing halogen atom size. Among the three CrX₃, CrI₃ exhibits the largest exchange splitting gap, which can be explained by a stronger intralayer Cr-Cr superexchange.

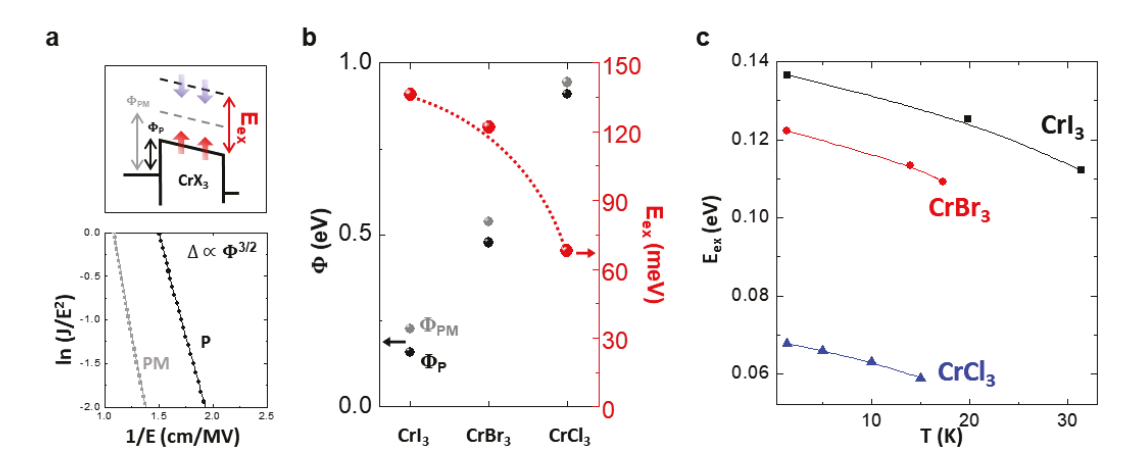


Figure S12. Magnetic exchange splitting gap of few-layer CrX₃. (a) Top: a schematic illustration of band structure for the calculation of splitting energy gap ($E_{ex} = 2(\Phi_{PM} - \Phi_P)$). Bottom: ln (J/E²) versus E⁻¹ plot of 10-layer CrI₃ at two different conditions (grey: 49K without field, black: 1.4K with B \perp ab = 5.5T). (b) Φ_{PM} and Φ_P for 10L CrI₃, 10L CrBr₃, and 12L CrCl₃ and deduced exchange splitting gap at 1.4K.

References

- 1. Kim, H. H., *et al.* One million percent tunnel magnetoresistance in a magnetic van der Waals heterostructure. *Nano Lett.*, **18**, 4885-4890 (2018).
- 2. Wang, L., *et al.* One-Dimensional Electrical Contact to a Two-Dimensional Material. *Science*, **342**, 614-617 (2013).
- 3. Lenzlinger, M., Snow, E. H. Fowler-Nordheim Tunneling into Thermally Grown SiO₂. *J. Appl. Phys.*, **40**, 278-283 (1969).
- 4. Zhang, W. B., Qu, Q., Zhua, P., Lam, C. H. Robust intrinsic ferromagnetism and half semiconductivity in stable two-dimensional single-layer chromium trihalides. *J. Mater. Chem. C*, **3**, 12457-12468 (2015).